Journal of Sol-Gel Science and Technology
https://doi.org/10.1007/s10971-025-06832-3

ORIGINAL PAPER

Synergistic effect of Al doping and sol-gel synthesis on the photocatalytic degradation of ciprofloxacin

Muhammad Yasar[1] · Aseel A. Kadhem[2] · Kinza Fatima[3] · Muhammad Sajid[4] · Muhammad Nauman Ullah[5] · Ammara Sattar[6] · Muzaffar Abbas[7] · Asad Riaz[8] · Shahid Ashraf[9]

Received: 22 October 2024 / Accepted: 26 May 2025

Abstract

This study is the first to investigate the photocatalytic degradation of ciprofloxacin using Al-doped Mn0.3Ba0.4C-d0.3AlxFe2-xO4 and examine the impact of Al doping on the photocatalytic properties of barium-manganese ferrites, as well as the structural, optical, surface area, and morphological properties of Mn0.3Ba0.4Cd0.3AlxFe2-xO4 (x = 0.0, 0.5) spinel ferrites. and their subsequent photocatalytic performance for ciprofloxacin degradation. The Al-doped ferrite achieved a 93.45% degradation efficiency, outperforming the undoped sample by 56.68%. This enhanced photocatalytic activity can be attributed to the synergistic effects of Al doping, which include a narrowed bandgap, increased surface area, reduced particle size, and modified electronic structure. Scavenger analysis revealed that hydroxyl radicals were the primary reactive species. Al doping decreased the bandgap from 2.2 eV to 1.9 eV and reduced crystallite size. FTIR spectroscopy indicated structural changes, with peak shifts in the tetrahedral and octahedral sites. SEM revealed a refined microstructure with smaller, uniform particles, reducing the average grain size from 61.72 nm to 50.33 nm. The BET surface area increased upon Al doping. Kinetic studies have shown that degradation follows pseudo-first-order kinetics. Photocatalyst Performance Assessment revealed improved quantum yield (5×10^{-9} molecules/photon) and space-time yield (2.50×10^{-10} molecules/photon/mg) for the Al-doped sample. The enhanced photocatalytic activity is attributed to the increased surface area, reduced particle size, and modified electronic structure owing to the Al doping. This study highlights the potential of Al-doped $Mn_{0.3}Ba_{0.4}Cd_{0.3}Al_xFe_{2-x}O_4$ (x = 0.0, 0.5) ferrites as efficient photocatalysts for ciprofloxacin degradation during water treatment.

✉ Muhammad Yasar
mayoyasar@gmail.com

[1] Institute Of Chemical Sciences, Bahauddin Zakariya University, Multan 60800 Punjab, Pakistan

[2] Ministry of Education, Wasit Education Directorate, Wasita Secondary School for Distinguished Students, Al-Kut, Iraq

[3] National Center for Nanoscience and Technology (NCNST), Chinese Academy of Sciences, Beijing 100190, China

[4] Institute of Microscale Optoelectronics, Optical Engineering, Shenzhen University, Shenzhen 518055 Guangdong, China

[5] Department of Chemical Engineering, School of Chemical and Materials Engineering (SCME), National University of Sciences & Technology (NUST), Islamabad 44000, Pakistan

[6] Department: department of physics, faculty of engineering and technology, (FEAS), Riphah international university islamabad, Islamabad 44000, Pakistan

[7] Department of Chemistry, Faculty of Science, Mahidol University, Rama VI road Phaya Thai, 10400 Bangkok, Thailand

[8] Department of Mechanical, Energy, Management and Transportation Engineering, University of Genova, Genova 16145, Italy

[9] Department of Physics, University of Agriculture Faisalabad, Faisalabad 38000, Pakistan

Published online: 10 June 2025

Graphical Abstract

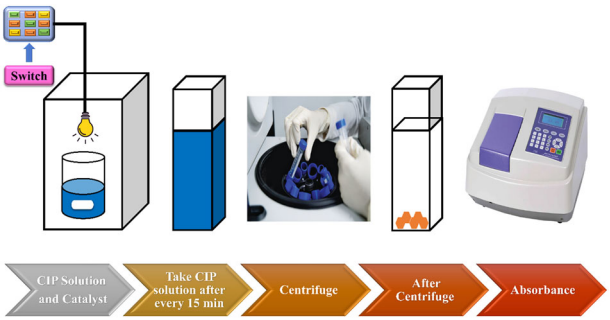

Keywords Spinel Ferrites · Aluminum Doping · Photocatalysis · Ciprofloxacin Degradation · Bandgap Engineering · Surface Area

Highlights

- Al-doped $Mn_{0.3}Ba_{0.4}Cd_{0.3}Al_xFe_{2-x}O_4$ ($x = 0.5$) achieved 93.45% ciprofloxacin degradation efficiency, significantly higher than the undoped sample (56.68%).
- Al doping reduced the bandgap from 2.2 eV to 1.9 eV, enhancing visible-light absorption and photocatalytic activity.
- The crystallite size decreased from 37.24 nm to 27.25 nm, and the BET surface area increased from 8.39 m^2/g to 32.14 m^2/g due to Al doping.
- SEM revealed smaller, uniform particles with an average grain size reduction from 61.72 nm to 50.33 nm in the Al-doped sample.
- Photocatalytic degradation followed pseudo-first-order kinetics ($R^2 = 0.987$), with hydroxyl radicals as the primary reactive species.

1 Introduction

In recent decades, the spread of pharmaceutical pollutants in aquatic systems has become a serious environmental concern. Ciprofloxacin, a common broad-spectrum antibiotic, is one of the contaminants that has drawn the most attention because of its persistence in aquatic habitats and its negative impacts on ecosystems and human health [1]. Ciprofloxacin, a widely used antibiotic in both human and animal healthcare, belongs to the fluoroquinolone class of antibiotics and is used to combat a range of bacterial infections. However, its widespread use has led to its ubiquitous presence in wastewater effluents, surface water, and drinking water [2, 3]. Ciprofloxacin is associated with several risks in aquatic environments. This fosters antibiotic-resistant bacteria and undermines medical treatment globally. Additionally, low concentrations disrupt aquatic ecosystems, affecting organism growth, reproduction, and behavior, potentially causing long-term ecological imbalances [4, 5]. Global regulatory agencies have established antibiotic limits for the water quality. The European Union permits a maximum of 0.1 µg/L of individual pharmaceuticals in drinking water. Detecting and removing ciprofloxacin at low concentrations is difficult in standard water treatment processes [6]. This underscores the need for advanced, efficient, and cost-effective technologies to degrade ciprofloxacin in water. Treatments for pharmaceutical pollution include adsorption, membrane filtration, biological treatments, and chemical oxidation. However, traditional methods often struggle with efficiency, cost, or the potential creation of harmful byproducts [7, 8].Advanced oxidation processes (AOPs), particularly heterogeneous photocatalysis, have gained prominence owing to their ability to degrade recalcitrant organic pollutants such as ciprofloxacin under mild conditions using solar energy. This process generates highly reactive species, mainly hydroxyl radicals (•OH), which can effectively mineralize various organic contaminants [9]. When a semiconductor photocatalyst is subjected to light with energy matching or exceeding its band gap, electron-hole pairs are typically produced during the photocatalytic reaction. The charge carriers migrate to the catalyst surface to engage in redox interactions with dissolved oxygen and adsorbed water, forming Reactive Oxygen Species (ROS), such as hydrogen peroxide (H_2O_2), hydroxyl radicals (•OH), and superoxide radicals (O_2•-). These ROS degrade organic pollutants such as ciprofloxacin into non-hazardous substances such as CO_2 and H_2O [10, 11].

The effectiveness of photocatalytic processes largely depends on the characteristics of the photocatalyst. Numerous photocatalysts, such as TiO_2, ZnO, WO_3, and

composite materials, have been examined for environmental degradation. TiO_2 has been extensively studied because of its high photocatalytic activity, low toxicity, and chemical stability [12]. However, their wide bandgap restricts visible-light utilization, which forms a significant part of the solar spectrum. This limitation has spurred efforts to develop new photocatalysts that better absorb visible light and have improved charge separation efficiencies [13–15].

Recently, spinel ferrites have emerged as promising materials for photocatalytic applications. This is due to their unique magnetic and electronic characteristics, coupled with their narrow bandgaps and exceptional chemical stability [16–20]. Barium-manganese ferrites exhibit potential for environmental applications, such as the degradation of organic pollutants. The substitution of Fe^{3+} ions with Al^{3+} ions in the ferrite structure enhances the photocatalytic activity by altering the electronic structure and surface properties [21–23].

In this study, Al-doped spinel ferrites were synthesized, characterized, and evaluated for ciprofloxacin degradation. The material was chosen due to its mixed valence states of Mn and Fe, which can enhance charge transfer and separation, potentially improving photocatalytic activity [24]. Incorporating Al^{3+} ions into the ferrite lattice can alter the electronic structure and optical properties, potentially narrowing the bandgap and enhancing visible-light absorption. Additionally, partially substituting Fe^{3+} with Al^{3+} is anticipated to introduce defects and modify the surface properties of the material, significantly impacting its photocatalytic performance [25, 26]. Al doping of $Mn_{0.3}Ba_{0.4}Cd_{0.3}Al_xFe_{2-x}O_4$ is expected to significantly alter its photocatalytic properties [27]. Al doping can enhance adsorption, reactivity, and light absorption by inducing structural changes, modifying chemical properties, and altering the electronic band structure [28, 29].

The incorporation of Al^{3+} ions into the Mn-Ba-Cd ferrite lattice significantly influences its photocatalytic properties. Key mechanisms include Al $^{3+}$ substitution reducing the bandgap energy, enhancing visible light absorption, and facilitating electron-hole pair generation. The introduction of intermediate energy levels within the bandgap acts as electron traps, hindering recombination and prolonging the lifetime of the charge carriers. The spatial separation of electrons and holes, facilitated by the complex electronic environment, enables efficient redox reactions with adsorbed water and oxygen, leading to the formation of highly reactive species, such as hydroxyl and superoxide radicals. The combined effects of bandgap narrowing, improved charge carrier dynamics, and enhanced ROS generation contribute to the superior photocatalytic performance of Al-doped Mn-Ba-Cd ferrite for ciprofloxacin degradation [30–32].

Spinel ferrites are superior photocatalysts owing to their broad light absorption, magnetic recoverability, and strong stability. Unlike TiO_2, they effectively utilize visible light and can be easily separated from the treated water, thereby ensuring their long-term efficacy in water treatment [33]. This study is the first to investigate the photocatalytic degradation of ciprofloxacin using Al-doped $Mn_{0.3}Ba_{0.4}Cd_{0.3}Al_xFe_{2-x}O_4$ and to examine the impact of Al doping on the photocatalytic properties of barium-manganese ferrites.

This study aimed to synthesize and characterize Al-doped $Mn_{0.3}Ba_{0.4}Cd_{0.3}Al_xFe_{2-x}O_4$ ($x = 0.0, 0.5$) and evaluate the photocatalytic degradation of ciprofloxacin under visible light. By correlating the structural, morphological, and optical properties with the photocatalytic performance, Al doping can be optimized to enhance the efficiency. Understanding these mechanisms can contribute to the development of high-performance photocatalysts for water remediation.

2 Materials and methods

2.1 Materials

This study exclusively used analytical-grade compounds, which were employed without additional purification processes. The following chemicals were acquired from Sigma-Aldrich: Ba $(NO_3)_2$ (99%), Mn $(NO_3)_2{\cdot}4H_2O$ (98%), Fe $(NO_3)_3{\cdot}$ $9H_2O$ (98%), and Al $(NO_3)_3$ · $9H_2O$ (98%). TCI Chemicals were used as the source of ciprofloxacin hydrochloride (≥98%). The ethanol used to prepare the ammonia solution was 99. A 9% ammonia solution was donated by Merck, whereas a 33% ammonia solution was obtained from Merck. Deionized water with a resistivity of 18.2 MΩ·cm was employed throughout all experimental trials.

2.2 Preparation of $Mn_{0.3}Ba_{0.4}Cd_{0.3}Al_xFe_{2-x}O_4$ ($x = 0.0$, 0.5) by sol–gel technique

The Barium manganese ferrite nanoparticles doped with aluminum, with a composition of $Mn_{0.3}Ba_{0.4}Cd_{0.3}Al_xFe_{2-x}O_4$ ($x = 0.0, 0.5$), were synthesized using the sol-gel auto-combustion method [34]. Stoichiometric quantities of barium nitrate (0.104 M), manganese nitrate tetrahydrate (0.078 M), iron nitrate nonahydrate (0.523 M), and aluminum nitrate nonahydrate (0.131 M for the $x = 0.5$ sample) were dissolved in deionized water. Citric acid was added as a chelating agent in a 1:1 molar ratio to the total metal ions. The pH of the solution was adjusted to 7.0 using a 33% ammonia solution. The sol-gel was formed at 90 °C for 4 h with constant stirring at 600 rpm. The resulting gel

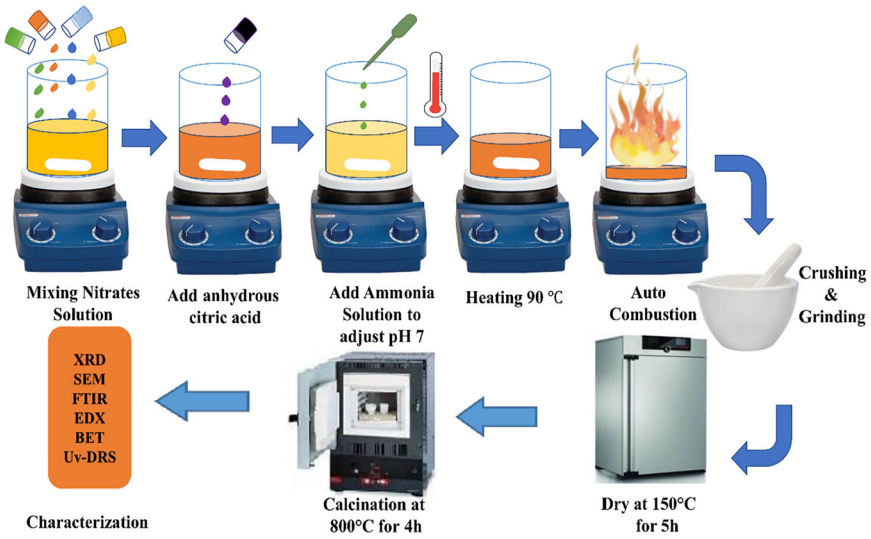

Fig. 1 Sol-gel method diagram

underwent auto-combustion to yield fluffy precursor powder. This powder was then ground using an agate mortar and pestle to obtain crystalline ferrite. The final product was calcined at 800 °C for 4 h with a heating rate of 5 °C/min and subsequent temperature plateaus at 200 °C for 1 h, 400 °C for 1 h, and 800 °C for 4 h. The samples were allowed to cool naturally to room temperature (Fig. 1).

2.3 Characterization of nanoparticles

Structural characterization involves X-ray diffraction (XRD) for crystal structure determination (Rigaku Ultima IV), Fourier Transform Infrared Spectroscopy (FTIR) for functional groups identification (Bruker Vertex 70), scanning electron microscopy (SEM) to determine surface morphology (JEOL JSM-IT200), energy-dispersive X-ray spectroscopy (EDX) for elemental composition analysis (Oxford Instrument AZtec Energy), and These two methods collectively are most advantageous to ascertain the property of the nanoparticle samples in terms of their physical and chemical requirements.

2.4 Photocatalytic activity investigations

A systematic investigation of the visible-light-driven photocatalytic degradation of ciprofloxacin was conducted using Mn0.3Ba0.4Cd0.3AlxFe2-xO4 (x = 0.0, 0.5) nanoparticles as photocatalysts. The photocatalytic reactions were carried out in a custom-designed photoreactor equipped with a 100 W xenon lamp and a Newport filter (≥420 nm), providing a spectral distribution of 420–800 nm. The light source was configured to deliver an intensity of 100 mW/cm^2 at the sample surface, with a beam diameter of 5 cm positioned 15 cm from the reaction solution. The experimental setup utilized a 250 mL capacity quartz reactor (6.5 cm diameter) containing 100 mL of reaction solution with a depth of 3 cm. Temperature control was maintained at 25 ± 1 °C using a water circulation cooling system. For each experimental run, 20 mg of the photocatalyst was dispersed in 100 mL of a 10 mg/L ciprofloxacin solution. The suspension was magnetically stirred at 400 rpm for 60 min under dark conditions to establish adsorption-desorption equilibrium prior to illumination. During the photocatalytic process, 3 mL aliquots were collected at 10-minute intervals and centrifuged at 4000 rpm for 5 min to separate the catalyst. The supernatant was analyzed using a Shimadzu UV-1800 UV-Vis spectrophotometer equipped with a 1 cm path length quartz cuvette, scanning from to 200–800 nm at 400 nm/min. The photocatalytic efficiency was calculated using Eq. (1).

$$\text{Degradation efficiency}(\%) = \frac{C_0 - C_t}{C_0} \times 100 \quad (1)$$

where C_0 is the initial concentration of ciprofloxacin and C_t is the concentration at time t.

Rigorous quality control measures were implemented throughout the experiment. Temperature was monitored using a K-type thermocouple (± 0.5 °C accuracy), while pH measurements were recorded using a calibrated pH meter (± 0.01 units). Light intensity was monitored every 30 min using a calibrated radiometer. Control experiments were conducted in parallel to evaluate the effects of adsorption and photolysis. The photocatalytic efficiency was calculated based on the ratio of the initial concentration (C0) to the concentration at time t (Ct). To assess the reusability, the photocatalysts were magnetically separated post-reaction, washed with deionized water and ethanol, dried at 60 °C, and reused in subsequent degradation cycles. The mechanistic investigation of the photocatalytic process included the analysis of reactive oxygen species (ROS)

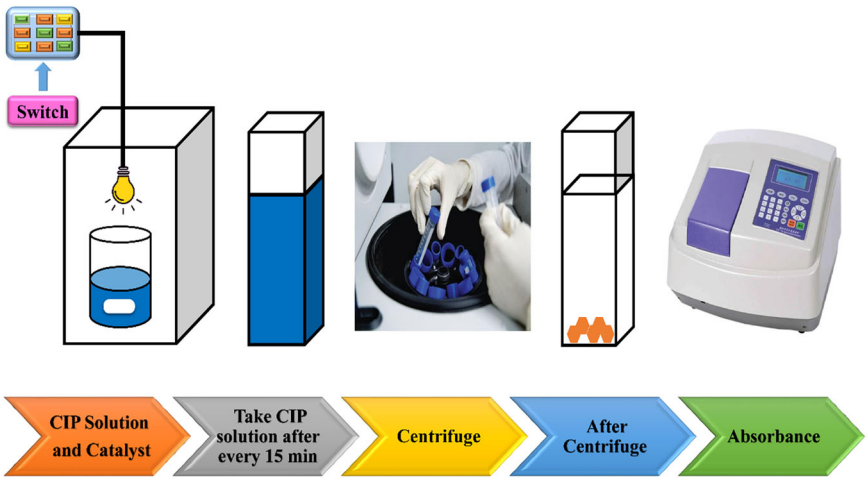

Fig. 2 the systematic diagram the photodegradation process of CIP [30]

using specific scavengers: tert-butyl alcohol for hydroxyl radicals, benzoquinone for superoxide radicals, and disodium ethylenediaminetetraacetate for holes. Additional parameters investigated included the effects of dye dose, catalyst loading, temperature, doping concentration, and solar light irradiation on the degradation efficiency (Fig. 2).

2.5 Electrical resistivity measurements

The electrical resistivities of $Mn_{0.3}Ba_{0.4}Cd_{0.3}Fe_2O_4$ and $Mn_{0.3}Ba_{0.4}Cd_{0.3}Al_{0.5}Fe_{1.5}O_4$ ferrite samples were measured using a standard four-probe technique. Pellet-shaped samples were prepared by pressing the powdered ferrites into discs and sintering them at 800 °C for 4 h. The sintered pellets were placed in a custom-built four-probe resistivity measurement cell. Platinum wire probes were brought into contact with the sample surface, and a Keithley 2400 Source Meter was used to apply a constant current through the outer probes while measuring the voltage drop across the inner probes. The electrical resistivity (ρ) was calculated using the following formula:

$$\rho = \frac{v}{I} \times \left(\frac{\pi \times \tau}{\ln(2)} \right)$$

Where V is the measured voltage, I is the applied current, and t is the thickness of the pellet sample. The measurements were carried out over a temperature range of 300–600 K, and the reciprocal temperature (1000/T) was plotted against the logarithm of the electrical resistivity (log ρ) to obtain the plots shown in the manuscript.

2.6 Kinetic studies

Time-dependent experiments were conducted to study the ciprofloxacin degradation kinetics using the $Mn_{0.3}Ba_{0.4}Cd_{0.3}Al_{0.5}Fe_{1.5}O_4$ photocatalyst under the following optimal conditions: pH 7, 30 °C, 10 ppm initial ciprofloxacin concentration, 20 mg catalyst dose, and 100 W visible light. Aliquots were taken at set intervals (0, 10, 20, 30, 40, 50, 60, 70, and 80 min), filtered through a 0.45 µm membrane to remove catalyst particles, and analyzed for ciprofloxacin concentration using a Shimadzu UV-1800 UV-Vis spectrophotometer at λmax = 275 nm. The kinetic data were examined using pseudo-first-order and pseudo-second-order kinetic models. Equation (2) represents a pseudo-first-order kinetic equation:

$$\ln\left(\frac{C_0}{C}\right) = K_1 t \tag{2}$$

where C_0 is the initial ciprofloxacin concentration, C is the concentration at time t, and k_1 is the pseudo-first-order rate constant. The pseudo-second-order kinetic equation was applied as follows in Eq. (3)

$$1/C = 1/C_0 + K_2 t \tag{3}$$

where k_2 is the pseudo-second-order rate constant. The applicability of each model was evaluated based on the linear regression coefficient (R^2) values. The rate constants (k_1 and k_2) were determined from the slopes of the respective linear plots.

2.7 Photocatalyst efficiency evaluation

To assess the practical effectiveness of various photocatalysts for removing ciprofloxacin, their energy usage during the catalytic process was examined. The essential performance metrics, including the quantum yield (QY), space-time yield (SY), figure of merit (FOM), and photon flux (Ph), were determined using the following formulae:

Quantum Yield (QY)

$$\mathrm{QY} = \frac{\text{Moles of Number of reacted molecules}}{\text{Number of absorbed photons}} \times 100 \quad (4)$$

Space-Time time Yield (SY)

$$\mathrm{SY} = \frac{\text{Mass of removed pollutant}}{\textit{catalyst mass} \times \text{reaction time}} \quad (5)$$

Figure of Merit (FOM).

$$\mathrm{FOM} = \frac{\text{Quantum Yield}}{\text{Space} - \text{Time Yield}} \quad (6)$$

Calculated Photon flux (Ph):

$$Ph = \frac{\textit{Light intensity}}{\textit{photon energy} \times \textit{Avogadro Number}} \quad (7)$$

These metrics offer substantive insights into the efficacy and sustainability of photocatalytic systems, facilitating the comprehensive evaluation of diverse photocatalysts and optimization of the treatment process.

3 Results and discussion

3.1 XRD analysis

The X-ray diffraction patterns of the $Mn_{0.3}Ba_{0.4}Cd_{0.3}Fe_2O_4$ and $Mn_{0.3}Ba_{0.4}Cd_{0.3}Al_{0.5}Fe_{1.5}O_4$ ferrites exhibited a cubic spinel structure with characteristic peaks corresponding to the (220), (311), (442), (511), (440), and (533) lattice planes. The peak at (311) in both materials demonstrated the highest intensity, indicating a single-phase cubic spinel structure with the Fd3m space group (Fig. 3(a)). Upon Al^{3+} substitution, a shift in the peak positions towards higher 2θ values was observed, consistent with the smaller ionic radius of Al^{3+} (0.57 ÅÅ) than that of Fe^{3+} (0.67 Å). Al doping also caused peak broadening and reduced intensity, suggesting alterations in the crystal structure. The crystallite size was determined using the Scherrer Eq. (8).

$$\mathrm{D} = \frac{\mathrm{K}\lambda}{\beta \cos\theta} \quad (8)$$

The crystallite size (D) was calculated using the shape factor (K), X-ray wavelength (λ), full width at half maximum (β), and Bragg angle (θ). The crystallite size decreased from 37.24 to 27.25 nm with Al doping, consistent with lattice contraction (Table 1). This reduction can be attributed to several factors: substitution of Al^{3+} for Fe^{3+} introduces lattice strain and defects that limit crystal growth; Al^{3+} presence alters the nucleation and growth kinetics during ferrite formation, favoring smaller crystallites; and lattice distortion from the size mismatch between Al^{3+} and Fe^{3+} creates smaller coherent domains. Thus, Al doping significantly affected the crystal structure and growth mechanism of the Ba-Mn ferrite system. The value of the lattice constant, denoted by "a" is calculated using the Eq. (9).

$$a = d\sqrt{h^2 + k^2 + l^2} \quad (9)$$

where h, k, and l are the Miller indices of the ferrite crystal planes, a is the lattice parameter, and "" is the interplanar spacing. The lattice parameter of the doped sample decreased from 8.472 to 8.380 Å compared to that of the undoped sample. This observation is consistent with the lower ionic radius of Al^{3+} (0. 0.57 Å) compared to that of Fe^{3+} (0. 0.67 Å Å), leading to shrinkage of the lattice structure [35]. The decrease in the lattice constant results in a corresponding reduction in the cell volume from 608.194 to 588.503 $Å^3$, calculated using Eq. (10)

$$v = a^3 \quad (10)$$

The d-spacing, determined by Bragg's law Eq. (11)

$$d = \frac{n\lambda}{2\sin\theta} \quad (11)$$

where n represents an integer value, λ denotes the wavelength, d refers to the lattice spacing, and θ represents the Bragg angle.), the d-spacing decreased from 2.5546 to 2.5267 Å, further confirming lattice contraction. The hopping lengths L_a and L_b, which represent the distance between magnetic ions, also decreased from 3.668 Å to 3.628 Å and from 2.995 Å to 2.962 Å, respectively, owing to the overall lattice shrinkage [36]. The incorporation of Al^{3+} into the Mn-Ba-Cd ferrite lattice resulted in a decrease in crystallite size from 37.24 nm to 27.25 nm. This reduction led to an increased surface area, facilitating greater adsorption of ciprofloxacin and enhancing the efficiency of photocatalytic reactions. Additionally, the smaller crystallite size reduced the charge carrier diffusion lengths, minimizing recombination and promoting the generation of reactive oxygen species. The substitution of larger Fe^{3+} ions with smaller Al^{3+} ions caused a shift in the XRD peak positions towards higher 2θ values, indicating lattice contraction. This structural modification alters the electronic band structure, potentially narrowing the bandgap and improving the visible light absorption. Furthermore, the lattice distortions and defects induced by the ionic size mismatch facilitated charge carrier separation and prolonged their lifetime, thereby enhancing photocatalytic activity.The combined effect of these structural modifications resulted in improved photocatalytic performance, as evidenced by the enhanced degradation of ciprofloxacin under visible light irradiation [37–39].

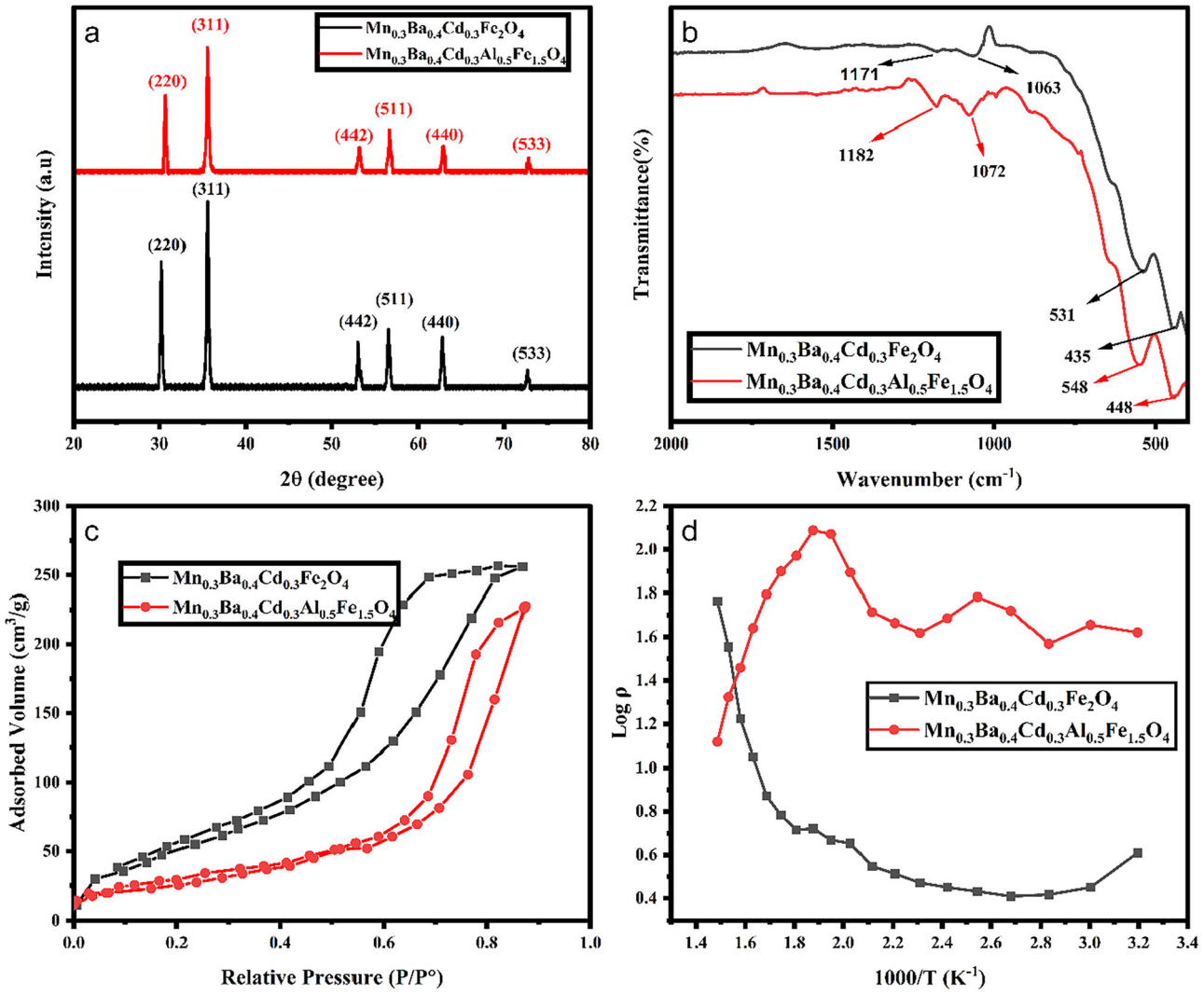

Fig. 3 Characterization of Mn $_{0.3}Ba_{0.4}Cd_{0.3}Fe_2O_4$ and $Mn_{0.3}Ba_{0.4}Cd_{0.3}Al_{0.5}Fe_{1.5}O_4$ (**a**) XRD Spectrum (**b**) FTIR Analysis (**c**) BET Analysis (**d**) Electrical Resistivity

Table 1 The XRD analysis of the crystal structure of $Mn_{0.3}Ba_{0.4}Cd_{0.3}Al_xFe_{2-x}O_4$ (x = 0.0, 0.5) (x = 0.0, 0.5) ferrite

Catalyst composition	FWHM	D-Spacing	Lattice constant (Å)	Cell Volume $(Å)^3$	Hoping length L_a (Å)	Hoping length L_b (Å)	Crystalline size (nm)
X = 0	0.2123	2.5546	8.4726	608.19	3.66872	2.99549	37.2495505
X = 0.5	0.2898	2.5267	8.3801	588.5	3.62869	2.96281	27.2577

3.2 FTIR characterization

The FTIR spectra of $Mn_{0.3}Ba_{0.4}Cd_{0.3}Fe_2O_4$ and $Mn_{0.3}Ba_{0.4}Cd_{0.3}Al_{0.5}Fe_{1.5}O_4$ were examined between 400 cm^{-1} and 4000 cm^{-1}, revealing the characteristic spinel ferrite absorption bands. Notably, two distinct absorption bands between 400 and 600 cm <> B-¹ were identified, corresponding to tetrahedral and octahedral site vibrations, respectively [40]. In the case of $Mn_{0.3}Ba_{0.4}Cd_{0.3}Fe_2O_4$, these characteristic peaks were observed at 531 cm^{-1} and 435 cm^{-1}, respectively, whereas in the Al-substituted sample, they shifted to 548 cm^{-1} and 448 cm^{-1}, respectively, owing to the substitution of Fe^{3+} by Al^{3+}. Higher wavenumber peaks were also detected: 1171 cm^{-1} and 1063 cm^{-1} for $Ba_{0.5}Mn_{0.5}Fe_2O_4$ and 1182 cm^{-1} and 1072 cm^{-1} for the Al-substituted sample, likely owing to residual FeO-OH groups and C-O stretching vibrations. The observed peak shifts towards higher wavenumbers can be attributed to the smaller ionic radius of Al3+ (0.57 Å) compared to Fe3+ (0.67 Å). The substitution of the larger Fe3+ cations by the smaller Al3+ cations in the spinel

structure leads to the contraction of the crystal lattice. These changes in the local coordination environment can affect the electronic structure, potentially leading to improved light absorption and charge carrier dynamics, which are crucial for enhanced photocatalytic activity. These findings confirmed the spinel structure and highlighted the impact of cation substitution on the molecular structure.

3.3 BET analysis

The nitrogen adsorption isotherms for the Mn $_{0.3}Ba_{0.4}Cd_{0.3}Fe_2O_4$ and $Mn_{0.3}Ba_{0.4}Cd_{0.3}Al_{0.5}Fe_{1.5}O_4$spinel ferrites revealed significant structural changes due to Al doping. The Al-doped sample showed markedly improved textural properties, with increases in BET surface area (8.39 to 32.14 m^2/g), total pore volume (0.028 to 1.18 cm^3/g), and average pore radius (10.38 to 34.26 Å), as shown in Table 2. Both samples exhibit Type IV isotherms, which are characteristic of mesoporous structures, with the Al-doped sample showing a more pronounced hysteresis loop, which is indicative of larger mesopores (Fig. 3(c)). The significant increases in the surface area, pore volume, and pore size indicate that Al doping notably changes the crystal structure and particle morphology of the spinel ferrite. These alterations, probably due to Al^{3+} replacing Fe^{3+}, may affect the catalytic properties of the material [41].

3.4 Electrical resistivity

The graph shows the electrical resistivity (log p) variation with reciprocal temperature (1000/T) for Mn $_{0.3}Ba_{0.4}Cd_{0.3}$-Fe_2O_4 and its Al-doped $Mn_{0.3}Ba_{0.4}Cd_{0.3}Al_{0.5}Fe_{1.5}O_4$ variants. The Al-doped sample exhibited higher resistivity across the temperature range, suggesting that Al incorporation increased the electrical resistivity (Fig. 3d). This increase is due to impurity scattering, the compensation effect, and potential barrier formation caused by Al doping. These resistivity changes influence photodegradation by potentially reducing charge recombination and extending charge carrier lifetimes, which may enhance photocatalytic activity. However, the decreased conductivity can hinder charge transport to the catalyst surface, possibly impeding redox reactions.

Table 2 Adsorption Description results of Nitrogen of the $Mn_{0.3}Ba_{0.4}Cd_{0.3}Al_xFe_{2-x}O_4$ (x = 0.0, 0.5)

Compositions	Bet Surface Area (m^2/g)	Total pore volume (cm^3/g)	Average pore radius (Å)
X = 0	8.39	0.028	10.38
X = 0.5	32.14	1.18	34.26

3.5 Scanning electron microscopy

Scanning electron microscopy (SEM) revealed significant microstructural changes in Mn $_{0.3}Ba_{0.4}Cd_{0.3}Fe_2O_4$ ferrite after Al doping. The undoped sample exhibited larger elongated particles with irregular morphologies and agglomeration tendencies (Fig. 4a). In contrast, Al-doped $Mn_{0.3}Ba_{0.4}Cd_{0.3}Al_{0.5}Fe_{1.5}O_4$ exhibited a refined microstructure with smaller, more uniform, and predominantly spherical particles, showing improved dispersion. This transformation is attributed to the incorporation of Al^{3+} ions, which inhibit grain growth and alter the crystallization dynamics. Al doping led to a more homogeneous particle distribution, reduced agglomeration, and increased the surface texture, as shown in Fig. 4(b). The average grain size decreased from 61.72 nm in the undoped samples to 50.33 nm in the Al-doped samples (*determined by the J Image Software*), respectively. Possible reasons for this reduction include impurity effects, solid-solution strengthening, secondary phase formation, and oxygen vacancy creation. These factors can disrupt atomic arrangements and pin grain boundaries, and impede grain formation and oxygen vacancy creation. These factors can disrupt the atomic arrangements, pin grain boundaries, and impede grain growth, resulting in a finer grain structure [42–44]. The smaller, more uniform particles with decreased average grain size from 61.72 nm to 50.33 nm provide a higher surface area and more accessible active sites for the adsorption of pollutants and the catalytic reactions.The improved dispersion and reduced agglomeration of the Al-doped ferrite particles can also enhance mass transport and light penetration, further promoting the photocatalytic degradation of ciprofloxacin.

3.6 EDX analysis

EDX analysis of the Mn $_{0.3}Ba_{0.4}Cd_{0.3}Fe_2O_4$ and $Mn_{0.3}Ba_{0.4}Cd_{0.3}Al_{0.5}Fe_{1.5}O_4$ samples provided insights into their elemental compositions and purities. For the undoped sample (Fig. 5a), peaks corresponding to Ba, Mn, Cd, Fe, and O were observed, reflecting their stoichiometric ratios. The Al-doped sample exhibited an additional Al peak and a reduced Fe peak, confirming the incorporation of Al into the ferrite structure at the expected atomic ratios (Fig. 5b). No impurity peaks were detected, indicating the high purity of the synthesized materials.

3.7 Optical properties

Incorporating aluminum as a dopant in Mn 0.3Ba0.4Cd0.3Fe2O4 results in a decrease in the bandgap from 2.2 eV to 1.9 eV, which leads to improved characteristics and catalytic efficacy under light exposure (Fig. 6).

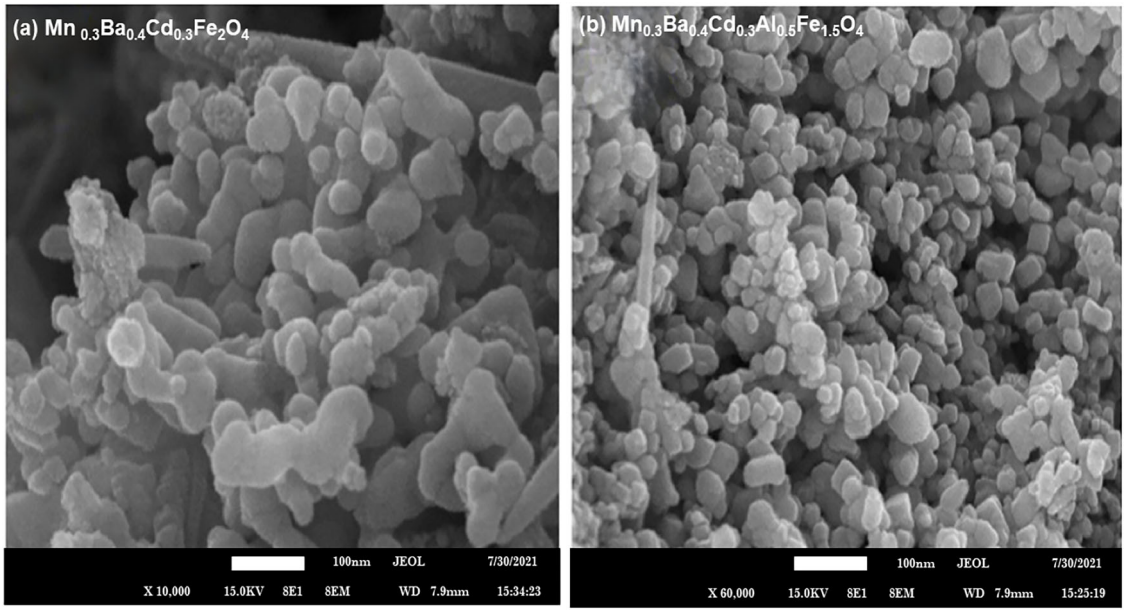

Fig. 4 Scanning electron microscopy (SEM) images of $Mn_{0.3}Ba_{0.4}Cd_{0.3}Al_xFe_{2-x}O_4$ (x = 0.0, 0.5) (**a**) and x = 0.5 (**b**), along with the grain size for x = 0.5 and x = 0

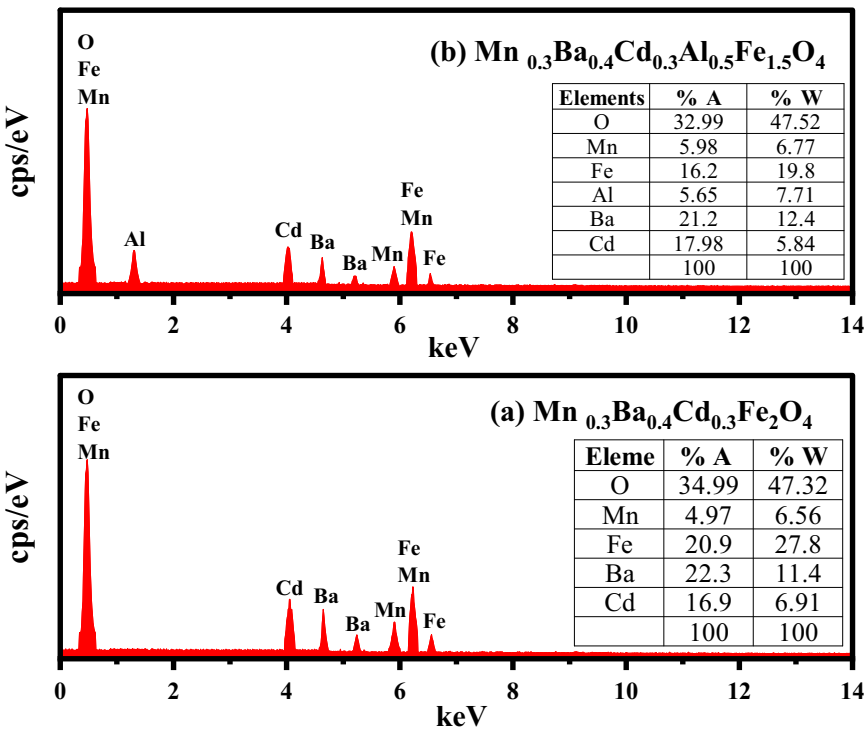

Fig. 5 The Edx Spectrum of (**a**) Mn $_{0.3}Ba_{0.4}Cd_{0.3}Fe_2O_4$ and (**b**) $Mn_{0.3}Ba_{0.4}Cd_{0.3}Al_{0.5}Fe_{1.5}O_4$

This change arises from crystal field effects, lattice distortion, intermediate energy levels, and charge transfer processes [45].

Al doping narrows the bandgap of iron oxides by distorting the lattice and altering the electronic band structure owing to the lower electronegativity of aluminum. The introduced intermediate energy levels act as electron traps or recombination centers, whereas the various oxidation states of aluminum ions facilitate charge transfer. This bandgap narrowing enhances visible-light-driven photocatalytic activity through increased light absorption, improved charge separation, and lowered band-edge potentials, thereby optimizing the photodegradation performance [46].

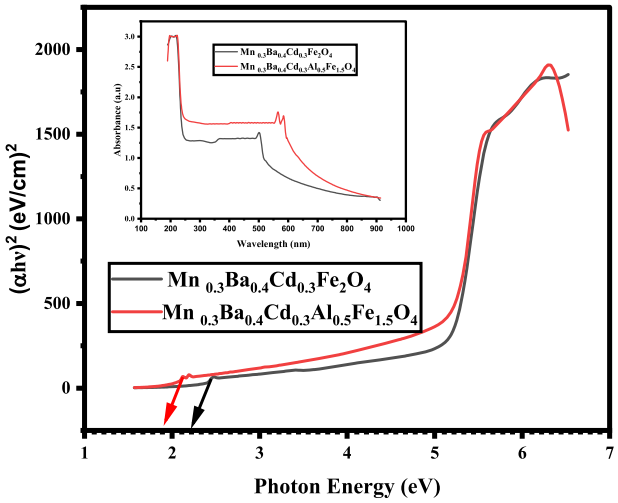

Fig. 6 The Uv-DRS spectrum for band gap determination

3.8 Photodegradation studies

3.8.1 Aluminum doping influences

The incorporation of aluminum (Al) into $Mn_{0.3}Ba_{0.4}Cd_{0.3}Al_xFe_{2-x}O_4$ (x = 0.0, 0.5) significantly enhanced the photodegradation efficiency of ciprofloxacin, increasing from 56.68% to 93.45% with higher Al doping (x = 0.0, 0.5), far exceeding that of photolysis alone (Fig. 7a). Al doping modifies the electronic band structure, enhances light absorption, and enables the catalyst to utilize a broader solar spectrum [47]. Al incorporation facilitates efficient charge carrier separation, reduces recombination losses, and extends the lifetime of the reactive species. Finally, the increased surface area due to Al doping offers more adsorption sites for ciprofloxacin, promoting proximity to the reactive sites of the photocatalyst and enhancing degradation. The catalyst with an Al doping concentration of x = 0.5 exhibited optimal performance, achieving the highest degradation rate [30].

3.8.2 Effect of pH

Impact of initial solution pH on ciprofloxacin photodegradation. Experiments at pH 3, 7, and 11 showed degradation efficiencies of 99.81, 93.45, and 71.47%, respectively, indicating a decline in efficiency with increasing pH (Fig. 7(b)). This trend was attributed to the speciation of ciprofloxacin and the catalyst surface charge. At low pH, ciprofloxacin is mainly in its cationic form, which interacts well with the catalyst surface. As the pH increases, changes in ciprofloxacin speciation and catalyst surface charge alter these interactions [32]. A higher pH initially enhances electrostatic attraction, but an excessive pH leads to competition between the hydroxyl ions and ciprofloxacin for the catalyst sites. These results underscore the importance of pH in optimizing ciprofloxacin photodegradation, with acidic conditions being the most effective [48].

3.8.3 Effect of ciprofloxacin concentration on enrofloxacin photodegradation

Effect of increasing ciprofloxacin concentration on enrofloxacin photodegradation. Experiments with ciprofloxacin concentrations of 10, 20, 30, and 40 mg/L showed enrofloxacin photodegradation efficiencies of 93.43, 83.65, 73.87, and 64.87%, respectively (Fig. 7c). An inverse relationship was observed between ciprofloxacin concentration and enrofloxacin degradation efficiency owing to competitive adsorption on the catalyst surface sites and scavenging of reactive species by ciprofloxacin. Both structurally similar fluoroquinolones compete for adsorption sites and reactive species, and higher ciprofloxacin concentrations intensify this competition and reduce enrofloxacin degradation [49].

3.8.4 Role catalyst quantity ciprofloxacin degradation

This section examines the impact of the catalyst dosage on ciprofloxacin photodegradation. Experiments using catalyst doses of 20, 40, 60, 80, and 100 mg yielded photodegradation efficiencies of 93.45, 97.28, 99, 100, and 74%, respectively, after 75 min (Fig. 7d). The showed an efficiency peak at 80 mg and a notable decrease at 100 mg, which was attributed to the enhanced active site availability at lower doses, reduced light penetration and scattering at higher doses, and possible catalyst aggregation at higher doses. The optimal catalyst dose of 90 mg balanced the increase in the number of active sites with minimal light obstruction, emphasizing the significance of optimizing the catalyst dosage in ciprofloxacin photodegradation for maximum efficiency.

3.8.5 Effect of temperature on ciprofloxacin photodegradation

Experiments were carried out at 20, 40, and 60 °C to examine how temperature influences the photocatalytic breakdown of ciprofloxacin. The degradation efficiency reached 93.45% at 20 °C. Increasing the temperature to 40 °C improved the efficiency to 98.17%, an increase of 4.72 percentage increase (Fig. 8(a)). Increasing the temperature to 60 °C increased the efficiency to 99.88%, a 6.43 percentage point improvement from room temperature, owing to the enhanced reaction kinetics, mass transfer, reduced activation energy, and synergistic thermal effects that complement photocatalytic degradation [50].

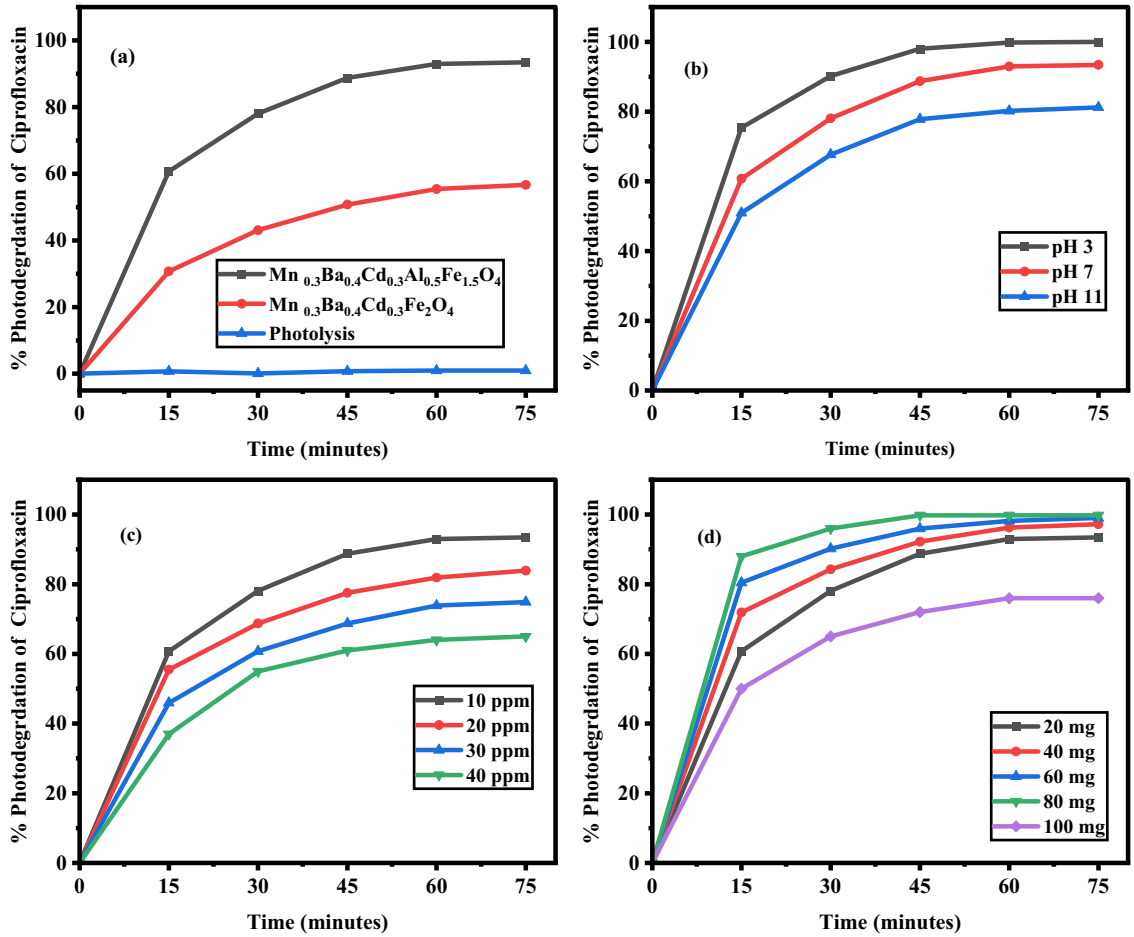

Fig. 7 Impact of ciprofloxacin photodegradation on (**a**) doping effects and photolysis, (**b**) pH effects, (**c**) pollutant dose effects, and (**d**) catalyst dose effects

3.8.6 Effect of light intensity and solar light

Effect of light intensity on ciprofloxacin photodegradation. Experiments conducted at 100 and 200 W under solar light revealed a clear correlation between increased light intensity and improved degradation efficiency (Fig. 8(b)). The ciprofloxacin degradation rates were 93.56% and 100% after 75 min at 100 W and 200 W, respectively, whereas complete degradation was achieved after 45 min under solar light. This trend resulted from increased photon absorption by the catalyst, faster reaction rates between ciprofloxacin and the reactive species, and the broad spectrum of solar light, offering more efficient wavelengths for catalyst activation [51]

3.8.7 Effect of H_2O_2 concentration on photodegradation

The percentage degradation of ciprofloxacin increased markedly with increasing H_2O_2 concentration from 0 to 9 mM (93.45% to 99.90%), showing a positive correlation between H_2O_2 concentration and photodegradation efficiency (Fig. 8c). When the H_2O_2 concentration increased to 12 mM, the degradation rate decreased to 80.61538%, suggesting that this concentration was ideal for achieving maximum photodegradation. H_2O_2, a source of highly reactive and potent hydroxyl radicals (•OH) under photolytic conditions, enhances photodegradation by increasing •OH generation. However, at higher concentrations, H_2O_2 acts as a radical scavenger, competing with the pollutant for •OH radicals, reducing their availability and decreasing photodegradation efficiency. Moreover, H_2O_2 can generate other reactive species, such as superoxide (O_2-*) and hydroperoxyl (HO_2-) radicals, contributing to the degradation process [52].

3.8.8 Scavenger analysis and identification of active species

Experiments using scavenging agents such as benzoquinone (BQ), ethylenediaminetetraacetic acid (EDTA), and tert-butanol (TBA) were conducted to determine the main reactive species responsible for the photocatalytic breakdown of ciprofloxacin. The baseline degradation efficiency

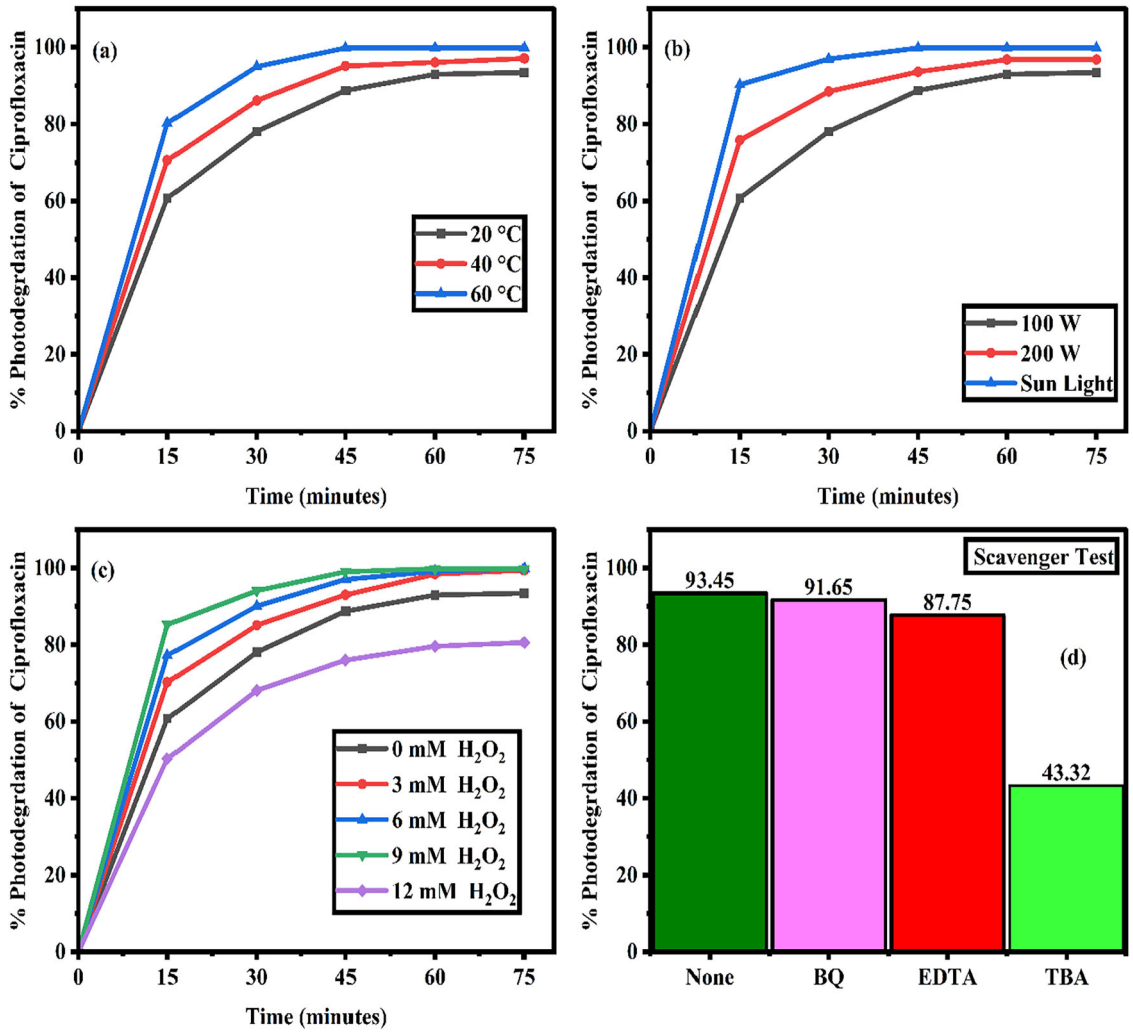

Fig. 8 Impact of ciprofloxacin photodegradation on (**a**) temperature, **b** light intensity vs. solar spectrum, **c** H_2O_2 addition, and **d** scavenger analysis

was 93.45%. BQ reduced the efficiency to 91.12%, indicating the minimal role of superoxide radicals (Fig. 8d). EDTA decreased the efficiency to 87.54%, suggesting a modest contribution from the holes. TBA significantly lowered the efficiency to 43.67% with hydroxyl radicals as the primary reactive species, causing a 49.78% reduction from the baseline. Thus, hydroxyl radicals mainly drive the photocatalytic degradation of ciprofloxacin, with minor contributions from holes and superoxide radicals [53].

3.8.9 Kinetic analysis

The ciprofloxacin degradation kinetics using the $Mn_{0.3}Ba_{0.4}Cd_{0.3}Al_{0.5}Fe_{1.5}O_4$ photocatalyst were assessed using pseudo-first-order and pseudo-second-order models. Linear regression analysis yielded R^2 values of 0.987 and 0.944 for the pseudo-first-order and pseudo-second-order models, respectively (Fig. 9a, b). The higher R^2 value for the pseudo-first-order model indicated a better fit to the data, suggesting that ciprofloxacin degradation predominantly followed pseudo-first-order kinetics under these conditions. This indicated that the degradation rate mainly depended on the ciprofloxacin concentration, with the other reactants remaining stable.

3.8.10 Possible Mechanism Photodegradation of Ciprofloxacin

The photocatalytic degradation of ciprofloxacin (CIP) using $Mn_{0.3}Ba_{0.4}Cd_{0.3}Al_{0.5}Fe_{1.5}O_4$ involves multiple stages. When exposed to light, the catalyst captures energy, generating electron-hole pairs that interact with oxygen and water to produce reactive oxygen species (ROS), primarily hydroxyl and superoxide radicals, as illustrated in Fig. 10. The photocatalytic degradation mechanism of ciprofloxacin (CIP) using $Mn_{0.3}Ba_{0.4}Cd_{0.3}Al_{0.5}Fe_{1.5}O_4$ was enhanced through the effects of Al doping. The substitution of Fe^{3+} with Al^{3+} significantly impacts the electron-hole pair dynamics and

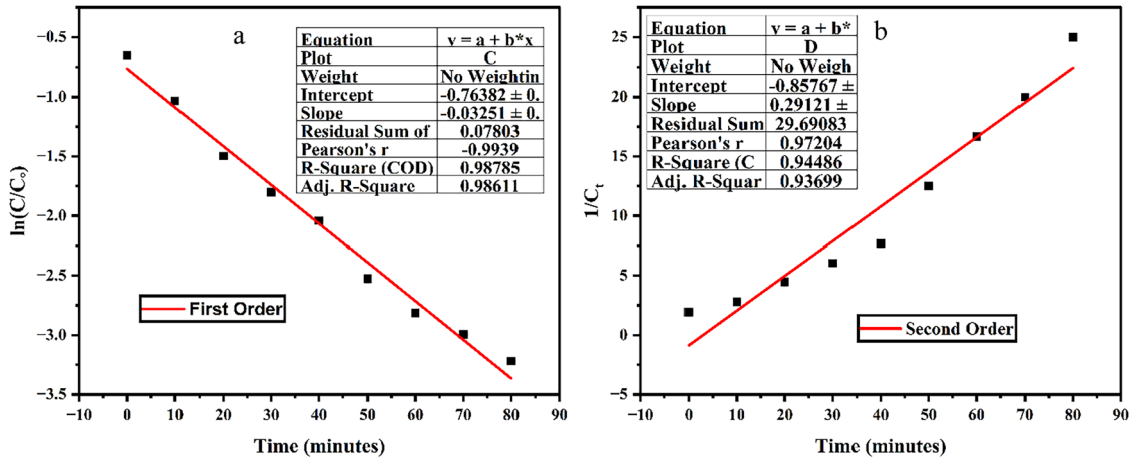

Fig. 9 Kinetics (**a**) First order (**b**) Second order

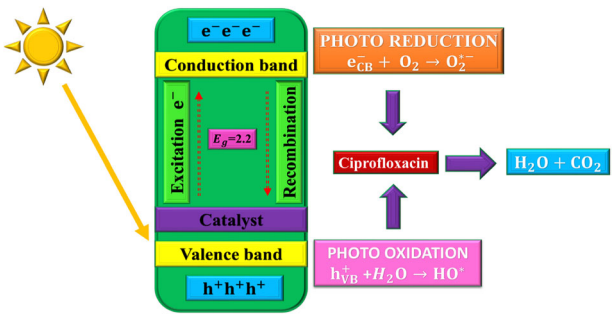

Fig. 10 Possible mechanism photodegradation of CIP

reactive oxygen species (ROS) generation. Specifically, Al doping introduces oxygen vacancies and surface defects that serve as electron traps, thereby reducing the recombination rates. Furthermore, the incorporation of Al^{3+} ions modify the band structure, leading to enhanced visible light absorption and improved charge carrier mobility. These modifications result in a more efficient generation of hydroxyl (•OH) and superoxide (O_2•−) radicals, which are the primary ROS responsible for CIP degradation. The photocatalytic process proceeds through four key steps, with Al doping effects playing a crucial role at each stage: (1) photon absorption, where Al doping narrows the bandgap and enables more efficient visible light capture; (2) ROS formation, where enhanced charge carrier separation promotes the generation of superoxide and hydroxyl radicals; (3) CIP oxidation, where the increased ROS concentration facilitates more effective degradation of CIP through hydroxylated intermediates; and (4) mineralization, where the process culminates in complete CIP conversion to CO_2, H_2O, and inorganic ions, with Al doping maintaining sustained photocatalytic activity through improved charge carrier dynamics [54–56] These ROS then engage with CIP and trigger oxidative breakdown through hydroxylated intermediates. This process ultimately leads to the complete mineralization of CIP, converting it into carbon dioxide, water, and inorganic ions.

1. ***Photon absorption*:** The catalyst absorbs light and generates electron-hole pairs.

$$Mn_{0.3}Ba_{0.4}Cd_{0.3}Al_{0.5}Fe_{0.5}O_4 + hv \rightarrow Mn_{0.3}Ba_{0.4}Cd_{0.3}Al_{0.5}Fe_{0.5}O_4(e^-, h^+) \quad (12)$$

2. **Reactive oxygen species (ROS) formation**: The interaction of electrons and holes with water and oxygen results in the formation of superoxide and hydroxyl radicals, respectively.

$$h^+ + H_2O/OH^- \rightarrow OH^* + H^+ \quad (13)$$

In aqueous solutions, electrons in the excited state within the conduction band interact with the dissolved oxygen molecules, resulting in the formation of superoxide radical anions. These potent oxidants can subsequently react to produce other ROS, including hydrogen peroxide (H_2O_2) and hydroperoxyl radicals (HO_2•).

$$e^- + O_2(aq) \rightarrow O_2^{*-} \quad (14)$$

The efficiency of this step depends on the ability of the catalyst to separate and sustain electron-hole pairs, preventing recombination. The mixed metal composition likely contributed to the improved separation.

3. **CIP oxidation:** ROS attack CIP molecules, forming hydroxylated intermediates and eventually breaking them down.

$$CIP + HO^*/O_2^- \rightarrow Hydroxyakted\ intemidate \rightarrow CO_2 + H_2O + Mineral\ acids \quad (15)$$

Table 3 Photocatalysts removal efficiency and quantum yield correlation

Photo-Catalyst Composition	Quantum efficiency (molec /photon)	Space Time Yield (molec /photon/mg)	FOM (L/g/mol/J/h)	References
$Mn_{0.3}Ba_{0.4}Cd_{0.3}Fe_2O_4$	3.04×10^{-09}	1.52×10^{-10}	4.22×10^{-16}	Current study
$Mn_{0.3}Ba_{0.4}Cd_{0.3}Al_{0.5}Fe_{1.5}O_4$	5×10^{-09}	2.50×10^{-10}	6.96×10^{-16}	Current study
$Sr_{0.2}Mn_{0.8}Fe_2O_4$	1.33×10^{-09}	1.33×10^{-8}	1.39×10^{-12}	[31]
$Sr_{0.2}Mn_{0.8}Al_{0.2}Fe_{1.8}O_4$	1.57×10^{-09}	1.57×10^{-8}	1.64×10^{-12}	[31]
$Sr_{0.2}Mn_{0.8}Al_{0.4}Fe_{1.6}O_4$	1.85×10^{-09}	1.85×10^{-8}	1.93×10^{-12}	[31]
$Sr_{0.2}Mn_{0.8}Al_{0.6}Fe_{1.4}O_4$	1.13×10^{-09}	1.13×10^{-8}	1.18×10^{-12}	[31]

4. **Mineralization**: This process results in the complete conversion of CIP into CO_2, H_2O, and inorganic ions. The mixed-metal-oxide composition of the catalyst enables visible-light absorption and efficient electron-hole separation. The overall reaction is summarized as follows:

$$\mathrm{CIP} + \mathrm{hv} + Mn_{0.3}Ba_{0.4}Cd_{0.3}Al_{0.5}Fe_{0.5}O_4 + \mathrm{O_2} + \mathrm{H_2O} \rightarrow \mathrm{CO_2} + \mathrm{H_2O} + \text{Mineral acids} + Mn_{0.3}Ba_{0.4}Cd_{0.3}Al_{0.5}Fe_{0.5}O_4 \quad (16)$$

This process effectively degrades organic pollutants into less harmful inorganic compounds [57].

3.8.11 Photocatalyst performance assessment

Table 3 presents a comparative analysis of the photocatalytic performance of two ferrite compositions, $Mn_{0.3}Ba_{0.4}Cd_{0.3}Fe_2O_4$ and $Mn_{0.3}Ba_{0.4}Cd_{0.3}Al_{0.5}Fe_{1.5}O_4$, for ciprofloxacin degradation under visible-light irradiation. The quantum yield represents the efficiency of the photocatalyst in converting absorbed photons into chemical reactions that degrade the target pollutant [58]. A higher quantum yield indicates a more efficient photocatalyst. The space-time yield provides a measure of the productivity of the photocatalyst per unit mass, taking into account both the quantum yield and the catalyst loading [59]. Compared to the Sr-based photocatalysts reported in [31], $Mn_{0.3}Ba_{0.4}Cd_{0.3}Fe_2O_4$ and $Mn_{0.3}Ba_{0.4}Cd_{0.3}Al_{0.5}Fe_{1.5}O_4$ photocatalysts studied in the current work show somewhat lower quantum yields and space-time yields. However, the figure of merit, which accounts for both the removal efficiency and the energy consumption, is still competitive. Further optimization of the catalyst composition and reaction conditions could potentially improve the quantum and space-time yields for the materials in the current study. Both catalysts were evaluated under visible light conditions for 75 min, using a 100 W lamp and a photocatalyst dosage of 0.02 g in a 0.01 g L^{-1} pollutant concentration. The aluminum-doped ferrite demonstrated superior performance, achieving a removal efficiency of 93.45% compared to 56.68% for the undoped ferrite. This enhancement is further reflected in the quantum yield (QY), with the Al-doped catalyst showing a higher value of 5×10^{-9} molecules $photon^{-1}$ than 3.04×10^{-9} the undoped variant. The space-time yield (STY) and figure of merit (FOM) also improved with aluminum doping, increasing from 1.52×10^{-10} to 2.5×10^{-10} molecules $photon^{-1}mg^{-1}$ and from 4.22×10^{16} to 6.96×10^{16} μmol L^{-1} h^{-2} g^{-1} W^{-1}, respectively. The incorporation of Al into the ferrite structure enhances its photocatalytic efficiency, potentially owing to the improved charge separation, increased surface area, and altered bandgap properties [36, 60].

3.8.12 Catalyst recyclability and deactivation of $Mn_{0.3}Ba_{0.4}Cd_{0.3}Al_{0.5}Fe_{1.5}O_4$

Reusability experiments indicated a reduction in the degradation efficiency of Al-doped Mn-Ba-Cd ferrite from 93.45% in the first cycle to 89% after five cycles (Fig. 11). Four primary factors contribute to this deactivation: Sintering and Agglomeration: High-temperature calcination and repeated cycling under illumination cause sintering and agglomeration of catalyst particles, reducing the surface area and active sites, thereby diminishing the photocatalytic performance. Leaching of Active Species: Partial dissolution and leaching of active metal ions (Al^{3+}, Mn^{2+}, Fe^{3+}) during photocatalytic reactions and washing steps result in gradual catalytic activity loss over multiple cycles. Catalyst Poisoning: Accumulation of reaction intermediates or byproducts on the catalyst surface blocks active sites and hinders pollutant adsorption, decreasing photocatalytic efficiency. Photo-corrosion: Prolonged light exposure and generation of reactive oxygen species partially degrade the ferrite material, further deactivating the photocatalyst. Strategies to enhance the long-term stability and reusability of Al-doped Mn-Ba-Cd ferrite photocatalysts include Surface Modification: Applying protective coatings or functionalizing the catalyst surface, such as incorporating silica or carbon-based shells, can improve structural and chemical stability. Reaction Condition Optimization: Optimizing the pH, temperature, and pollutant concentration can minimize harmful intermediates and reduce catalyst deactivation during repeated use. Post-treatment Regeneration: Effective

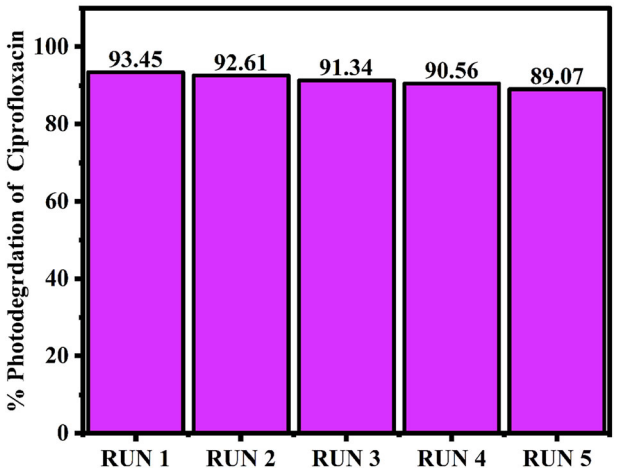

Fig. 11 The reusability of $Mn_{0.3}Ba_{0.4}Cd_{0.3}Al_{0.5}Fe_{1.5}O_4$ catalyst

regeneration methods, such as thermal treatment or acid/base washing, can restore catalytic activity by removing accumulated deposits and recovering active sites. Structural Modifications: Alternative synthesis methods or doping strategies, such as incorporating additional cations or using core-shell architectures, may enhance the intrinsic stability of the ferrite structure and long-term performance [61, 62].

4 Conclusion

Al-doped $Mn_{0.3}Ba_{0.4}Cd_{0.3}Al_xFe_{2-x}O_4$ ($x = 0.0, 0.5$) ferrites were synthesized and characterized for ciprofloxacin degradation. Al-doped ferrite achieved 93.45% degradation efficiency compared to 56.68% for undoped. Hydroxyl radicals were the primary reactive species, with a 49.78% reduction in efficiency when scavenged. The addition of 9 mM H_2O_2 increased the degradation rate to 99.90%. Bandgap decreased from 2.2 eV to 1.9 eV with Al doping. XRD analysis showed a crystallite size reduction from 37.25 nm to 27.26 nm due to Al doping. FTIR spectroscopy indicated peak shifts, with tetrahedral and octahedral site peaks shifting from 531 and 435 cm^{-1} to 548 and 448 cm^{-1}, respectively. SEM revealed smaller, uniform particles, reducing the average grain size from 61.72 nm to 50.33 nm. BET surface area increased from 8.39 m^2/g to 32.14 $m^2/$ kinetic studies showed degradation followed pseudo-first-order kinetics ($R^2 = 0.987$) more closely than pseudo-second-order ($R^2 = 0.944$). Photocatalyst Performance Assessment revealed improved quantum yield (5×10^{-9} molecules/photon) and space-time yield (2.50×10^{-10} molecules/photon/mg) for the Al-doped sample. The enhanced photocatalytic activity is attributed to the increased surface area, reduced particle size, and modified electronic structure. This study highlights the potential of $Mn_{0.3}Ba_{0.4}Cd_{0.3}Al_{0.5}Fe_{1.5}O_4$ ferrites for ciprofloxacin degradation during water treatment.

Future research directions for Al-doped Mn0.3Ba0.4Cd0.3AlxFe2-xO4 ($x = 0.0, 0.5$) ferrite photocatalyst systems. We have incorporated a discussion of potential research avenues in the revised manuscript. This study highlights several key areas for future investigation: scaling up the sol-gel auto-combustion synthesis method for industrial viability, assessing photocatalytic performance under varied environmental conditions (pH, temperature, and water matrix constituents), and exploring co-doping strategies with transition metals and rare-earth elements to enhance light harvesting and charge carrier separation efficiency. These systematic investigations will contribute to advancing the practical implementation of this photocatalyst system in water treatment applications.

Data availability

No datasets were generated or analysed during the current study.

Author contributions Muhammad Yasar: Conceptualization, data curation, writing—original draft preparation Aseel A. Kadhem.; methodology, Kinza Fatima. and Muhammad Sajid.; software, validation, Muhammad Nauman Ullah. and Ammara Sattar.; formal analysis, Muzaffar Abbas: resources, Asad Riaz and Shahid Ashraf: investigation, visualization.

Compliance with ethical standards

Conflict of interest The authors declare no competing interests.

References

1. Dhiman P, Rana G, Kumar A, Sharma G, Vo D-VN, AlGarni TS, Naushad M, ALOthman ZA (2021) Nanostructured magnetic inverse spinel Ni–Zn ferrite as environmental friendly visible light driven photo-degradation of levofloxacin. Chem Eng Res Des 175:85–101
2. John S, Rathinavelu S, Mary SMS, Nambi IM, Babu SM, Thomas T, Singh S (2023) Solar-driven hybrid photo-Fenton degradation of persistent antibiotic ciprofloxacin by zinc ferrite-titania heterostructures: degradation pathway, intermediates, and toxicity analysis. Environ Sci Pollut Res 30:39605–39617
3. Liu W, Zheng J, Ou X, Liu X, Song Y, Tian C, Rong W, Shi Z, Dang Z, Lin Z (2018) Effective extraction of Cr (VI) from hazardous gypsum sludge via controlling the phase transformation and chromium species. Environ Sci Technol 52:13336–13342
4. Al-Musawi TJ, Mengelizadeh N, Alwared AI, Balarak D, Sabaghi R (2023) Photocatalytic degradation of ciprofloxacin by MMT/CuFe2O4 nanocomposite: characteristics, response surface methodology, and toxicity analyses,. Environ Sci Pollut Res 30:70076–70093
5. Patangia DV, Anthony Ryan C, Dempsey E, Paul Ross R, Stanton C (2022) Impact of antibiotics on the human microbiome and consequences for host health. Microbiologyopen 11:e1260

6. Papagiannaki D, Belay MH, Gonçalves NP, Robotti E, Bianco-Prevot A, Binetti R, Calza P (2022) From monitoring to treatment, how to improve water quality: The pharmaceuticals case. Chem Eng J Adv 10:100245
7. Loganathan P, Vigneswaran S, Kandasamy J, Cuprys AK, Maletskyi Z, Ratnaweera H (2023) Treatment trends and combined methods in removing pharmaceuticals and personal care products from wastewater—a review. Membranes 13:158
8. Shan Z, Yang Y, Shi H, Zhu J, Tan X, Luan Y, Jiang Z, Wang P, Qin J (2021) Hollow dodecahedra graphene oxide-cuprous oxide nanocomposites with effective photocatalytic and bactericidal activity. Front Chem 9:755836
9. Li S, Yang Y, Zheng H, Zheng Y, Jing T, Ma J, Nan J, Leong YK, Chang J-S (2022) Advanced oxidation process based on hydroxyl and sulfate radicals to degrade refractory organic pollutants in landfill leachate. Chemosphere 297:134214
10. Batool I, Albalawi K, Khan AU, Tahir K, Khan ZUH, Zaki ME, Saleh EAM, Alabbad EA, Althagafi TM, Abdulaziz F (2023) The construction of novel CuO/SnO2@ g-C3N4 photocatalyst for efficient degradation of ciprofloxacin, methylene blue and photoinhibition of bacteria through efficient production of reactive oxygen species. Environ Res 231:116086
11. Liu W, Huang F, Wang Y, Zou T, Zheng J, Lin Z (2011) Recycling Mg (OH) 2 nanoadsorbent during treating the low concentration of CrVI. Environ Sci Technol 45:1955–1961
12. Somwanshi, SB, Somvanshi, SB & Kharat, PB (2020). Visible light driven photocatalytic activity of TiO2 nanoparticles prepared via gel-combustion process. Paper presented at the *Journal of Physics: Conference Series*. https://doi.org/10.1088/1742-6596/1644/1/012042
13. Jiang L, Zhou S, Yang J, Wang H, Yu H, Chen H, Zhao Y, Yuan X, Chu W, Li H (2022) Near-infrared light responsive TiO2 for efficient solar energy utilization. Adv Funct Mater 32:2108977
14. Wang Q, Pornrungroj C, Linley S, Reisner E (2022) Strategies to improve light utilization in solar fuel synthesis. Nat Energy 7:13–24
15. Li J, Arif N, Lv T, Fang H, Hu X, Zeng YJ (2022) Towards full-spectrum photocatalysis: extending to the near-infrared region. ChemCatChem 14:e202200361
16. Dastjerdi OD, Shokrollahi H, Mirshekari S (2023) A review of synthesis, characterization, and magnetic properties of soft spinel ferrites. Inorg Chem Commun 153:110797
17. Jadhav SA, Somvanshi SB, Khedkar MV, Patade SR, Jadhav K (2020) Magneto-structural and photocatalytic behavior of mixed Ni–Zn nano-spinel ferrites: visible light-enabled active photodegradation of rhodamine B. J Mater Sci: Mater Electron 31:11352–11365
18. Andhare, D, Jadhav, S, Khedkar, M, Somvanshi, SB, More, S & Jadhav, K (2020). Structural and chemical properties of ZnFe2O4 nanoparticles synthesised by chemical co-precipitation technique. Paper presented at the *Journal of Physics: Conference Series*. https://doi.org/10.1088/1742-6596/1644/1/012014
19. Jadhav SA, Raut AV, Khedkar MV, Somvanshi SB, Jadhav K (2022) Photocatalytic activity of nickel ferrite nanoparticles synthesized via sol-gel auto combustion method. Adv Mater Res 1169:123–127
20. Jadhav SA, Somvanshi SB, Gawali SS, Zakde K, Jadhav K (2024) Rare earth-doped mixed Ni–Cu–Zn ferrites as an effective photocatalytic agent for active degradation of Rhodamine B dye. J Rare Earths 42:488–496
21. Solyman S, Zaki H, Soliman S (2022) Investigation of structural, magnetic and electrical properties of aluminum substituted Co-Mg ferrite. Mater Chem Phys 279:125723
22. Anukool W, El-Nabulsi RA, Dabagh S, Almessiere M, Ashiq MGB, Guner S, Baykal A (2022) Effects of aluminum substitution on the microstructure and magnetic properties of cobalt ferrites prepared by the co-precipitation precursor. Appl Phys A 128:713
23. Manjunatha M, Reddy GS, Mallikarjunaiah K, Ramesh K, Bhat S (2022) Effect of aluminum substitution on structural and magnetic properties of nickel ferrites: Raman and 57Fe IFNMR studies. Ceram Int 48:23946–23954
24. Cheng Y, Zhang S, Wang Z, Wang B, You J, Guo R, Zhang H (2023) Review on spinel ferrites-based materials (MFe2O4) as photo-Fenton catalysts for degradation of organic pollutants. Sep Purif Technol 318:123971
25. Shashanka H, Saha S, Haritha K, Anantharamaiah P, Ramana C (2023) Aluminum and Zinc Co-substituted cobalt ferrite: structural, magnetic, and magnetostrictive properties. J Phys Chem C 127:11218–11230
26. Dilshad M, Khan HM, Zahid M, Honey S, Assiri MA, Imran M (2022) Structural, optical and dielectric properties of aluminum-substituted SrAl2 x Fe12-2 x O19 x=(0.0, 0.2, 0.4, 0.6, 0.8, 1.0) M-type hexagonal ferrites. J Mater Sci: Mater Electron 33:21519–21530
27. Singh G, Ubhi MK, Jeet K, Singla C, Kaur M (2023) A review on impacting parameters for photocatalytic degradation of organic effluents by ferrites and their nanocomposites. Processes 11:1727
28. Zhou Y, Xu B, Jiang T, Dong Z, Wu J, Lin Y, Chen Y, Zhong S (2023) Eco-friendly and economical preparation of permanent ferrite magnet with ultrapure magnetite concentrate: Focus on the action mechanism of silicon and aluminum impurities. Sep Purif Technol 311:123233
29. Trinadh B, Suresh J, Patta G, Babu KV, Komali C, Babu BV, Devi KA, Mohan BS, Samatha K (2023) Structural, optical, electrical and magnetic properties of aluminum substituted Co–Cu–Zn nanocrystalline ferrites. Solid State Commun 376:115360
30. Yasar, M & Javed, K (2024) Synthetic studies of aluminum-doped Zn0. 5Mn0. 5AlxFe2− xO4 ferrite for photocatalytic degradation of atrazine under visible light, *Arabian Journal for Science and Engineering*, 1-14. https://doi.org/10.1007/s13369-024-09442-3
31. Yasar, M & Kadhem, AA (2024) Investigating the Role of Aluminum Doping on the Bandgap Modulation and Photocatalytic Efficiency of Strontium Nickel Ferrites for Ciprofloxacin Degradation, *Arabian Journal for Science and Engineering*, 1-15. https://doi.org/10.1007/s13369-024-09604-3
32. Yasar M, Nazir R, Noreen F (2024) Synthesis, characterization, and photocatalytic activity of aluminum-doped nickel manganese ferrite for the photodegradation of methylene blue. React Kinet, Mechanisms Catal 137:505–521
33. Shakir, I, Basha, B, Alsaiari, NS, Arshad, J, Alrowaili, Z, Naeem, M, Al-Buriahi, M & Manzoor, A (2024) Mg doped Zinc Manganese Spinel Ferrite: Fabrication and Investigation of the Structural and Photocatalytic Properties, *Journal of the Indian Chemical Society*, 101194. https://doi.org/10.1016/j.jics.2024.101194
34. Yasar, M & Javed, K (2024) Synthetic Studies of Aluminum-Doped Zn0.5Mn0.5AlxFe2−xO4 Ferrite for Photocatalytic Degradation of Atrazine Under Visible Light, *Arabian Journal for Science and Engineering*. https://doi.org/10.1007/s13369-024-09442-3
35. Kumar KV, Paramesh D, Reddy PV (2015) Effect of aluminium doping on structural and magnetic properties of Ni-Zn ferrite nanoparticles. World J Nano Sci Eng 5:68
36. Anukool W, El-Nabulsi RA, Dabagh S (2023) Effect of Al3+ doping on dielectric properties of cobalt ferrite nanoparticle for using in high frequency applications,. J Sol-Gel Sci Technol 105:405–415
37. Lee HJ, Kim JH, Park SS, Hong SS, Lee GD (2015) Degradation kinetics for photocatalytic reaction of methyl orange over Al-doped ZnO nanoparticles. J Ind Eng Chem 25:199–206

38. Thejaswini T, Prabhakaran D, Maheswari MA (2016) Soft synthesis of potassium co-doped Al–ZnO nanocomposites: a comprehensive study on their visible-light driven photocatalytic activity on dye degradation. J Mater Sci 51:8187–8208
39. Zhao D, Chen C, Wang Y, Ma W, Zhao J, Rajh T, Zang L (2008) Enhanced photocatalytic degradation of dye pollutants under visible irradiation on Al (III)-modified TiO2: structure, interaction, and interfacial electron transfer. Environ Sci Technol 42:308–314
40. Jain R, Gulati S (2023) Influence of Fe2+ substitution on FTIR and Raman spectra of Mn ferrite nanoparticles,. Vibrational Spectrosc 126:103540
41. Chanoi ZA, Reyes VI, Martinez-Espinoza LA, Shafirovich E (2023) Toward a tunable fabrication of multifunctional iron-aluminum spinels via solution combustion synthesis: The effects of fuel, heating mode, and Fe: Al precursor ratio. Ceram Int 49:39049–39058
42. Junaid M, Kousar I, Gulbadan S, Khan MA, Yousuf MA, Baig MM, Ashraf GA, Somaily H, Morsi M (2022) Structural, microstructural, spectral, and dielectric properties of erbium substituted spinel ferrites. Phys B: Condens Matter 641:414120
43. Hasan M, Ali S, Khan M, Rizwan M, Zulqarnain M, Hussain A (2023) Structural, optical, electrical and magnetic tuning based on Zn substitution at a site in yttrium doped spinel ferrites. Mater Chem Phys 301:127538
44. Mahajan H, Godara SK, Srivastava A (2022) Synthesis and investigation of structural, morphological, and magnetic properties of the manganese doped cobalt-zinc spinel ferrite. J Alloy Compd 896:162966
45. Rahman M, Ullah MH, Tabassum S, Hoque M, Harun-Or-Rashid M (2024) Rietveld refined structural and sintering temperature dependent electromagnetic properties of Al3+ substituted Ni–Co ferrites prepared through sol–gel auto combustion method for high-frequency and microwave devices,. J Mater Sci: Mater Electron 35:952
46. Junaid M, Jan HA, Batoo KM, Jabeen R, Hussain S (2023) Band–gap reduction of aluminum substituted M− type hexagonal ferrite to study its characteristics. Results Chem 6:101133
47. Yasar, M, Mujtaba, A, Fatima, K, Rubab, M, Usman, M, Khan, MJ, Rao, DP & Sajjad, RW (2024) Synthesis, characterization, and photocatalytic activity of aluminum doped spinel ferrite nanoparticles for the photodegradation of Congo red, *Reaction Kinetics, Mechanisms and Catalysis*, 1-23. https://doi.org/10.1007/s11144-024-02714-x
48. Feng X, Dong C, Wang X, Wang J (2022) Mechanochemical treatment for degradation of ciprofloxacin (CIP) in solutions. Water Sci Technol 86:1958–1968
49. Lu C, Gu J, Wei G, Ba J, Zhang L, Li Z, Pei R, Li J, Wei J (2022) Three-dimensional electro-Fenton degradation of ciprofloxacin catalyzed by CuO doped red mud particle electrodes: Influencing factors, possible degradation pathways and energy consumption. J Environ Chem Eng 10:107737
50. Noroozi R, Gholami M, Farzadkia M, Jonidi Jafari A (2022) Degradation of ciprofloxacin by CuFe2O4/GO activated PMS process in aqueous solution: performance, mechanism and degradation pathway. Int J Environ Anal Chem 102:174–195
51. Gao H, Wang S, Wang Y, Yang H, Fang L, Chen X, Yi Z, Li D (2022) Fabrication and characterization of BaMoO4-coupled CaWO4 heterojunction micro/nanocomposites with enhanced photocatalytic activity towards MB and CIP degradation. J Electron Mater 51:5230–5245
52. Zhang J, Liu M, Pang B, Liu C, Ma J, Niu J, Zhang R (2023) Ciprofloxacin degradation in microbubble ozonation combined with electro-generated H2O2 process: Operational parameters and oxidation mechanism. Sep Purif Technol 325:124676
53. Fauzi A, Jalil A, Hassan N, Aziz F, Azami M, Abdullah T, Kamaroddin M, Setiabudi H (2022) An intriguing Z-scheme titania loaded on fibrous silica ceria for accelerated visible-light-driven photocatalytic degradation of ciprofloxacin. Environ Res 211:113069
54. De La Pena O, Aguayo A, De Coss R (2002) Effects of Al doping on the structural and electronic properties of Mg 1− x Al x B 2. Phys Rev B 66:012511
55. Pathak SK, Abate A, Ruckdeschel P, Roose B, Gödel KC, Vaynzof Y, Santhala A, Watanabe SI, Hollman DJ, Noel N (2014) Performance and stability enhancement of dye-sensitized and perovskite solar cells by Al doping of TiO2. Adv Funct Mater 24:6046–6055
56. Ancy K, Bindhu M, Bai JS, Gatasheh MK, Hatamleh AA, Ilavenil S (2022) Photocatalytic degradation of organic synthetic dyes and textile dyeing waste water by Al and F co-doped TiO2 nanoparticles. Environ Res 206:112492
57. Shah P, Joshi K, Shah M, Unnarkat A, Patel FJ (2022) Photocatalytic dye degradation using nickel ferrite spinel and its nanocomposite. Environ Sci Pollut Res 29:78255–78264
58. Purohit B, Jeanneau E, Guyot Y, Amans D, Mahler B, Joubert M-F, Dujardin C, Ledoux G, Mishra S (2023) Incorporation of Upconverting LiYF4: Yb3+, Tm3+ Nanoparticles with High Quantum Yield in TiO2 Metallogels for Near Infrared-Driven Photocatalytic Dye Degradation. ACS Appl Nano Mater 6:2310–2326
59. Balarabe BY, Maity P, Teixeira ACS, Iwarere SA (2023) h-BN nanosheet-modified Ag2WO4 nanocomposite for improved photocatalytic dye removal: insights into catalyst stability and reusability. Inorg Chem Commun 158:111560
60. Abuilaiwi FA, Awais M, Qazi UY, Ali F, Afzal A (2022) Al3+ doping reduces the electron/hole recombination in photoluminescent copper ferrite (CuFe2− xAlxO4) nanocrystallites. Boletín de la Soc Española de Cerámica y Vidr 61:252–262
61. Acharya R, Pati S, Parida K (2022) A review on visible light driven spinel ferrite-g-C3N4 photocatalytic systems with enhanced solar light utilization. J Mol Liq 357:119105
62. Rahman M, Hasan N, Hoque M, Hossen M, Arifuzzaman M (2022) Structural, dielectric, and electrical transport properties of Al3+ substituted nanocrystalline Ni-Cu spinel ferrites prepared through the sol–gel route,. Results Phys 38:105610